

# Numerical Simulation of Magnetic Nano Drug Targeting in Patient-Specific Lower Respiratory Tract <sup>☆</sup>

Flavia Russo<sup>a</sup>, Andrea Boghi<sup>b,\*</sup>, Fabio Gori<sup>a</sup>

<sup>a</sup>*Department of Mechanical Engineering, University of Rome "Tor Vergata", Via del politecnico 1, 00133 Rome, Italy*

<sup>b</sup>*School of Water, Energy and Environment, Cranfield University, Cranfield, Bedfordshire MK43 0AL, United Kingdom*

---

## Abstract

Magnetic nano drug targeting, with an external magnetic field, can potentially improve the drug absorption in specific locations of the body. However, the effectiveness of the procedure can be reduced due to the limitations of the magnetic field intensity. This work investigates this technique with the Computational Fluid Dynamics (CFD) approach. A single rectangular coil generates the external magnetic field. A patient-specific geometry of the Trachea, with its primary and secondary bronchi, is reconstructed from Digital Imaging and Communications in Medicine (DICOM) formatted images, throughout the Vascular Modelling Tool Kit (VMTK) software. A solver, coupling the Lagrangian dynamics of the magnetic nanoparticles with the Eulerian dynamics of the air, is used to perform the simulations. The resistive pressure, the pulsatile inlet velocity and the rectangular coil magnetic field are the boundary conditions. The dynamics of the injected particles is investigated without and with the magnetic probe. The flow field promotes particles adhesion to the tracheal wall. The particles volumetric flow rate in both cases has been calculated. The magnetic probe is shown to increase the particles flow in the target region, but at a limited extent. This behavior has been attributed to the small particle size and the probe configuration.

**Keywords:** Magnetic Hydro Dynamics, Patient-Specific, nanoparticles, Lagrangian model, Eulerian model, Lower respiratory tract.

---

## 1. Introduction

The lung cancer, a malignant tumor, is the first cause of death among common cancers, with the World Health Organization reporting a number of death of 1.5 million during 2012 [1]. The disease strikes mainly men, 16.7% of the

---

<sup>☆</sup>Nano Drug Targeting in Lower Respiratory Tract

\*A. Boghi

Email address: a.boghi@cranfield.ac.uk (Andrea Boghi )

total, with the highest estimated age-standardized incidence rate in Central, Eastern Europe and Eastern Asia. The incidence is lower among women, with the highest estimated rates in Northern America and Northern Europe [2]. It appears impossible to prevent this disease, although the incidence can be reduced by avoiding the main risk factors, such as smoking and air pollution. Treatment and long term outcomes rely on the type of cancer, the stage when is treated and the patients health. Chemotherapy, surgery and radiotherapy, are the most commonly used treatments, despite their numerous hazardous side effects.

In the last decade, new technologies have been developed in order to resolve these issues. In the magnetic therapy the drugs are guided directly into the interested organs, reducing the drug absorption in the tissues which are not interested by the tumor. Lungs represent an ideal target for drug delivery, due to the direct access and the large area exposed to drugs [3]. Different types of nanoparticles to enhance drug delivery have been studied in [4]. Mouse lungs have been investigated in [5] where a large number of leukocytes have been found in the lungs parenchyma and in the bronchiole lumen, suggesting they were attracted by the magnetic nanoparticles present.

Several Computational Fluid Dynamics (CFD) studies have been carried out to investigate blood flow [6–12] and the effect of nanoparticles embedded in the air flow. Nano and micro particles deposition, after the construction of idealized airway geometries, have been studied in [13] in order to find the optimal particle diameter for drug targeting. The transport and deposition of nanoparticles for cyclic and steady flow at low Reynolds numbers, have been studied in [14] by evaluating the mass transfer due to nanoparticles dispersion. The inspiratory flow in a three-generation symmetric bifurcation, under the assumption of low Reynolds numbers has been investigated in [15], while the turbulent flow has been investigated with the  $k - \omega$  model in [16]. Two breathing conditions, the resting/normal and the maximal one, have been studied in [17] by employing a patient specific geometry. The secondary flow fields and the inertial effects in patient specific lung geometries, obtained from Computed Tomography (CT) data set has been studied in [18]. Other studies focused on subject specific boundary conditions [19] and on the application of CFD to the surgery field in order to evaluate the flow rates in patients with bidirectional anastomosis [20]. The particle deposition in the lungs has been investigated in [21], by using two different geometry models in order to analyze the best regions where the deposition mechanism was higher.

Biological effects of electromagnetic fields have been investigated in [22], while the application of the magnetic technique for the transport of drugs and tracers in specific targets has been developed in [23]. Few CFD studies have been conducted to simulate the magnetic drug targeting in blood vessels both in idealized [24–27] and patient-specific [28, 29] geometries. A mathematical model has been proposed in [30] in order to investigate the deposition of magnetic particles aerosol in lung alveolus, by considering only one alveolus with a simplified spherical geometry. A particles diameter of  $5\mu m$  and a quadrupolar Halbach permanent magnet array have been used for that study.

51 The present study investigates the fluid dynamics of air inside the lower  
52 respiratory tract, where nanoparticles, used for drug targeting, are aerosolized,  
53 inhaled and dragged from the trachea to the bronchiole by an external mag-  
54 netic field. A patient-specific geometry is reconstructed from a data set of CT  
55 scan images of a middle-aged healthy man. The air is treated as a continuum  
56 medium with an Eulerian formulation, while a Lagrangian approach is used for  
57 the nanoparticles. A rectangular coil is the source of the external magnetic field  
58 with a current intensity which complies with the clinical standards. The results  
59 of the simulations without and with the magnetic probe are compared.

## 60 2. Materials and Methods

### 61 2.1. Domain reconstruction

62 The domain's geometry is generated with the open-source software VMTK  
63 (The Vascular Modeling Toolkit) [31], which reconstructs a real chest surface,  
64 with the trachea and its primary and secondary bronchi, from a DICOM series  
65 of images. The lungs are divided into left and right, which can be further  
66 divided into upper, lower and central lobes. The geometry takes into account  
67 the principal and secondary bronchial tubes, belonging to the upper and central  
68 lobes of the right lung, whereas the interested regions of the left one are located  
69 in the lower lobe. The magnetic field is applied to the upper lobe of the right  
70 lung, where the tumor is supposed to be. Because of the chest geometry, the axis  
71 of the magnetic probe is directed towards the left side of the abdomen. Since  
72 the procedure is operator-dependent, the non-interesting structures and artifacts  
73 are removed manually. The *Level Set* algorithm is applied to reconstruct the  
74 surface of interest [32, 33], which is refined with the *Parametric Deformable*  
75 *Models*, initialized with the *Colliding Front* methodology. The output of the  
76 *Level Set* algorithm is an image, and the *Marching Cubes* algorithm is used to  
77 reconstruct the surface, due to the depth of the interested geometry.

78 Flow extensions of cylindrical shape, equal to 6 times its diameter, are added  
79 to the inlets and the outlets of the domain to ensure that the flow, entering and  
80 leaving the computational domain, is fully developed. This approach allows to  
81 use standard boundary conditions (BC) to solve the partial differential equations  
82 (PDE) governing the phenomenon. The computational grid is generated once  
83 the flow extensions are added. An adaptive mesh is employed with a more refined  
84 grid close to the wall and in the smaller branches. The computational grid  
85 employs tetrahedral elements, with minimum and maximum dihedral angles,  
86 set up in order to reduce the skew angle and the number of non-orthogonal  
87 cells. Four grids are generated with different number of elements, respectively  
88 144,712 (grid1), 514,723 (grid2), 853,982 (grid3) and 1,245,423 (grid 4), to verify  
89 that the numerical solutions are grid-independent [15, 16].

90 The domain is shown in Fig.(1), where Fig.(1,a) presents the reconstruction  
91 obtained with the application of the Marching Cubes algorithm, while Fig.(1,b)  
92 labels the segments whose drug uptake is monitored during the numerical sim-  
93 ulations.

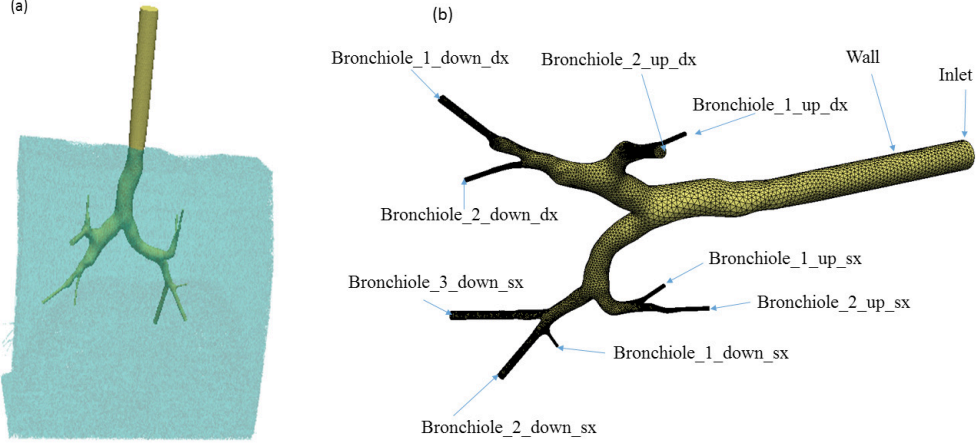


Figure 1: (a) Application of the Marching Cubes algorithm to obtain a reconstruction of the Trachea with its collateral structures; (b) Detail of the geometry used in this study.

## 2.2. Eulerian Model

The Magneto Hydro Dynamic (MHD) mathematical description is based on the coupling between the Navier-Stokes and the Maxwell equations. The MHD equations can be written for incompressible flow of air as follows:

$$\text{div}(\vec{v}_a) = 0 \quad (1)$$

$$\frac{\partial \vec{v}_a}{\partial t} + (\vec{v}_a \cdot \nabla) \vec{v}_a = -\frac{1}{\rho_a} \nabla p + \nu_a \nabla^2 \vec{v}_a + \vec{g} + \frac{1}{\rho_a \mu_0} \text{curl}(\vec{B}) \times \vec{B} \quad (2)$$

$$\frac{\partial \vec{B}}{\partial t} + (\vec{v}_a \cdot \nabla) \vec{B} = (\vec{B} \cdot \nabla) \vec{v}_a + \frac{1}{\sigma_a \mu_0} \nabla^2 \vec{B} \quad (3)$$

where the subscript  $a$  denotes “air”,  $\nu_a$  is the kinematic viscosity,  $\rho_a$  the density,  $\mu_0$  the magnetic permeability in the vacuum,  $\sigma_a$  the electric conductivity,  $\vec{g}$  the gravity acceleration,  $p$  the static pressure,  $\vec{v}_a$  the velocity field, and  $\vec{B}$  the magnetic induction field. As above mentioned, the air has been considered as an incompressible fluid. This is due to the fact that in physiological condition the velocity of the air is much smaller than the speed of sound and therefore the Mach number is much smaller than 1, and the fluid can be considered incompressible [34].

The air-momentum equation, Eq.(2), does not take into account the particles-air momentum transfer, because for particle volume fraction smaller than  $10^{-6}$

the disperse phase does not influence the continuum face, in agreement with [35, 36]. The effect of the magnetic field on the free ions and the erythrocytes is taken into account by the Lorentz force in Eq.(2).

The particle diameter used in this work is 5nm, which is typical of gold/iron-oxide nanoparticles [37, 38], and the particle geometry is spherical. Other shapes can be used, and their effect on the fluid flow is documented in the literature [39–41], but they are not considered here, because the Lagrangian model used is not suitable for non-spherical particles.

### 2.3. Lagrangian Model

Let us consider a particle of diameter  $d_p$ , velocity  $\vec{v}_p$ , and mass  $m_p$ , whose center position is  $\vec{x}_p$ . In a Lagrangian frame of reference, the position of each particle is obtained by the integration of its velocity,

$$\frac{d\vec{x}_p}{dt} = \vec{v}_p \quad (4)$$

which is evaluated from the momentum conservation equation, written as

$$\begin{aligned} \frac{d\vec{v}_p}{dt} = & - \underbrace{\frac{1}{\tau_p} \left( \vec{v}_p - \vec{v}_a + \frac{d_p^2}{12} \nabla^2 \vec{v}_a \right)}_{(I)} + \underbrace{\left( 1 - \frac{\rho_a}{\rho_p} \right) \vec{g}}_{(II)} + \underbrace{\frac{\rho_a}{\rho_p} \left( \frac{\partial \vec{v}_a}{\partial t} + (\vec{v}_a \cdot \nabla) \vec{v}_a \right)}_{(III)} + \\ & \underbrace{\frac{1}{2} \frac{\rho_a}{\rho_p} \left( \frac{\partial \vec{v}_a}{\partial t} + (\vec{v}_a \cdot \nabla) \vec{v}_a - \frac{d\vec{v}_p}{dt} \right)}_{(IV)} + \underbrace{\left( \frac{q_p}{m_p} \vec{v}_p - \frac{1}{\rho_p \mu_0} \text{curl}(\vec{B}) \right) \times \vec{B}}_{(V)} \end{aligned} \quad (5)$$

where  $\rho_p = 6m_p/\pi d_p^3$ , (I) is the drag, (II) the buoyancy, (III) the carrier phase inertia, (IV) the added mass and (V) the Lorentz force. The particle-particle interactions is neglected in Eq.(5) because of the small volume of the particles, which reduces the probability of collision. Furthermore,  $q_p$  is the electric charge of the particle and  $\tau_p$  the relaxation time, defined as

$$\tau_p = \frac{4}{3} \frac{\rho_p d_p}{\rho_b C_d |\vec{v}_b - \vec{v}_p|} \quad (6)$$

The standard definition of the drag coefficient, according to [42], is the following

$$C_d = \begin{cases} \frac{24}{\text{Re}_p} & \text{Re}_p < 0.1 \\ \frac{24}{\text{Re}_p} \left( 1 + \frac{1}{6} \text{Re}_p^{2/3} \right) & 0.1 < \text{Re}_p < 1000 \\ 0.44 & \text{Re}_p > 1000 \end{cases} \quad (7)$$

where the particle Reynolds number is defined as

$$\text{Re}_p = \frac{d_p |\vec{v}_b - \vec{v}_p|}{\nu_b} \quad (8)$$

#### 129 2.4. Boundary Conditions (BC)

130 The solution of the Eulerian system requires appropriate boundary condi-  
 131 tions (BC). A non-slip BC is imposed for the velocity on the wall. As far as the  
 132 outlets are concerned, a mixed BC is employed: when the air leaves the domain  
 133 the velocity normal derivative is set to zero, whereas the tangential velocity is  
 134 set to zero when air enters through the boundary. The velocity profile is imposed  
 135 on the inlet with a parabolic profile in steady state, while a Womersley-Evans  
 136 profile is employed in unsteady state, in analogy with [10, 29],

$$v_a(t, \xi) = 8 \frac{Q}{\pi D^2} (1 - \xi^2) + 2\Re \left( \sum_{n=1}^N V_n \Phi(\tau_n, \xi) e^{j\omega_n t} \right) \quad (9)$$

137 where

$$\Phi(\tau_n, \xi) = \frac{J_0(\tau_n) - J_0(\tau_n \xi)}{J_0(\tau_n) - 2J_1(\tau_n)/\tau_n} \quad (10)$$

138 and

$$\tau_n = j^{\frac{3}{2}} \frac{D}{2} \sqrt{\frac{\rho}{\mu_\infty}} \omega_n = j^{\frac{3}{2}} \alpha_n \quad (11)$$

139 Being  $r$  the radial coordinate,  $D$  the tracheal diameter,  $Q$  the volumetric flow  
 140 rate,  $\xi = 2r/D$ ,  $J_0$  and  $J_1$  the zeroth and first-order Bessel functions of the first  
 141 kind,  $\alpha_n$  the Womersley numbers of order  $n$ ,  $\Re()$  the real part of a complex  
 142 number,  $j = \sqrt{-1}$ ,  $V_n$  the Fourier coefficients of the pulsatile mean velocity  
 143 profile and the number of harmonics used to reproduce the flow rate. By using  
 144 the Fast Fourier Transform (FFT) algorithm, the first ten Fourier coefficients  
 145 of the flow rate in the trachea, derived from experimental data [17–19], are  
 146 employed to reconstruct the velocity profile.

147 The physiological waveform is reported in Fig.(2). The flow rate is pulsatile  
 148 and the Reynolds number varies from 0 to 2536, meaning that the flow is lam-  
 149 inar mostly and becomes transitional only at the peaks of the inhalation and  
 150 exhalation phases. For this reason the flow is treated as laminar, in agreement  
 151 with [14, 15].

152 As far as the pressure in the unsteady state is concerned, the resistive BC,  
 153 derived in [9, 20], is imposed on all the outlets

$$p = p_a + RQ \quad (12)$$

154 being  $p_a$  the reference pressure in the alveoli and  $R$  the hydraulic resistance.  
 155 The value of the resistance and the reference pressure are extrapolated from  
 156 the steady state simulations by imposing the volumetric flow rates and a zero  
 157 normal derivative condition for the pressure on the outlets.

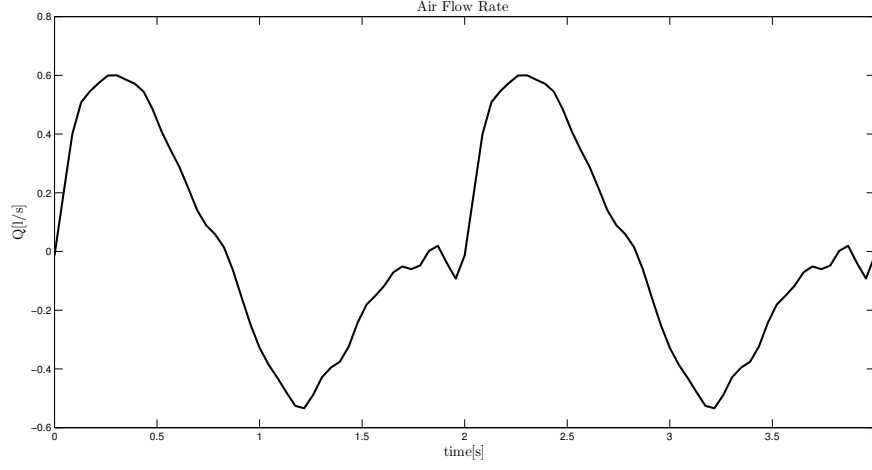


Figure 2: Pulmonary Flow Rate vs time.

## 158 2.5. Magnetic Induction BC

159 The Boundary Conditions for the magnetic induction field are zero normal  
 160 derivatives everywhere, except on the wall, where the magnetic field of the probe  
 161 is imposed. The external magnetic field is generated by a single rectangular coil,  
 162 with a negligible cross section of the wire, where an electric current is flowing.  
 163 This single rectangular coil is quite common in the clinical practice [43–46].

164 An analytical expression for the magnetic induction field is derived in [47].  
 165 A point in the coil reference frame, whose origin is at its centre, is identified  
 166 by the coordinates  $(x', y', z')$ . The coil dimensions are  $2a_1$  along the  $x'$  axis  
 167 and  $2b_1$  in the  $y'$  direction, with a section of  $2.5\text{cm}^2$ . The axis is normal of the  
 168 coil surface. The axis  $z'$  is normal of the coil surface. The components of the  
 169 magnetic induction field are

$$B_{x'} = \frac{\mu_0 I_1}{4\pi} \sum_{a=1}^4 \left[ \frac{z'(-1)^{a+1}}{r_a [r_a + d_a]} \right] \quad (13)$$

$$B_{y'} = \frac{\mu_0 I_1}{4\pi} \sum_{a=1}^4 \left[ \frac{z'(-1)^{a+1}}{r_a [r_a + C_a(-1)^{a+1}]} \right] \quad (14)$$

$$B_{z'} = \frac{\mu_0 I_1}{4\pi} \sum_{a=1}^4 \left[ \frac{d_a(-1)^a}{r_a [r_a + C_a(-1)^{a+1}]} - \frac{C_a}{r_a [r_a + d_a]} \right] \quad (15)$$

170 with

<i>Normal</i>	<i>CoilCoords(m)</i>	<i>TargetCoords(m)</i>	$\vec{B} _{1cm}(\text{mT})$
$n_x = -0.082166$	$x_c = -0.054377$	$x_t = 0.0314$	0
$n_y = 0.93057$	$y_c = -0.0891$	$y_t = -0.3554$	0
$n_z = 0.35677$	$z_c = -0.21683$	$z_t = 0.9342$	46.21

Table 1: Source and target coordinates; values for the normal to the chest surface of the patient; intensity of the Magnetic field along the  $z'$ - axis.

$H_D(\text{cm})$	$W_D(\text{cm})$	$D_D(\text{cm})$	$D_{M-T}(\text{cm})$	$T_O(\text{s})$	$\text{Re}_{\max}$
31.6	10.0	2.0	12.32	2.0	2536

Table 2: Simulation Parameters:  $H_D$  (domain height),  $W_D$  (domain width),  $D_D$  (domain depth),  $D_{S-T}$  (magnet-tumor distance),  $T_O$  (observation time),  $\text{Re}_{\max}$  (max tracheal Reynolds number).

$$\left\{ \begin{array}{l} C_1 = -C_4 = a_1 + x' \\ C_2 = -C_3 = a_1 - x' \\ d_1 = d_2 = y' + b_1 \\ d_3 = d_4 = y' - b_1 \\ r_a = \sqrt{C_a^2 + d_a^2 + z'^2} \end{array} \right. \quad (16)$$

The magnetic probe is located 1cm above the patient skin, in order that its modulus is smaller than 1.5 T. This is the limit allowed in clinical treatments [3, 4], since higher values can cause damage to the patient. The centre of the probe and the target are aligned with the  $z'$  axis. The target of the magnetotherapy is located at the upper lobe of the right lung because the maximum magnetic field must be concentrated on it.

The external chest surface of the patient is reconstructed using VMTK, with the procedure previously illustrated for the trachea. Two geometries are located in the same reference frame, in order to calculate the coordinates of the probe and the target. The dimensions of the rectangular coil, the current intensity and the positions of coil and target are reported in Tab.(1), while the main simulation parameters are listed in Tab.(2).

## 2.6. Numerical Details

The numerical simulations are performed with the software OpenFOAM, which solves the governing equations through the Finite Volume Method (FVM). The present problem has been solved with the **mhdB4Foam** solver, developed in [29], which couples the Lagrangian particle dynamics with the Eulerian MHD. Some Boundary Conditions, such as the resistive BC, the pulsatile profile on the inlet for unsteady state and the parabolic profile for steady state, are implemented through the utility **groovyBC**, in analogy with [29]. Furthermore, the



imposed magnetic field on the domain has been set using the `rectMagProbe` external OpenFOAM module, developed in [29]. The simulations are carried on for 2 respiratory cycles, considering a period of 1s and a variable time step, in order to guarantee a Courant number smaller than 0.5 during the respiratory cycle.

### 3. Results and Discussion

#### 3.1. Steady State

The steady state simulations are carried out until convergence is reached with the `simpleFoam` solver of OpenFOAM, which solves the Navier-Stokes equations in steady state. The numerical results, obtained with the four meshes, grid1, grid2, grid3 and grid4, are compared by using the `mapFields` utility, which maps the fields from one grid to another. The wall shear stress (WSS), defined as

$$\tau_{wall} = \hat{i}_{axis} \cdot \rho_a \nu_a ([I] - \hat{n}_{wall} \otimes \hat{n}_{wall}) \left( [\nabla \vec{v}_a] + [\nabla \vec{v}_a]^T - \frac{2}{3} \text{div}(\vec{v}_a) [I] \right)_{wall} \hat{n}_{wall} \quad (17)$$

is used to evaluate the grid independence. The contours of WSS are shown in Fig.(3). The WSS does not change significantly from grid1 to grid4. Therefore, grid2 is employed to perform the unsteady simulations, being a compromise between speed of execution and accuracy.

Figure 3 shows smaller WSS in the Trachea, due to the small velocity gradient, growing in the primary bronchi and reaching the maximum in the secondary bronchi. At the entrance of the secondary bronchi, the WSS increases, due to the section reduction. In a circular pipe the WSS is inversely proportional to the cubed radius. The increased number of branches reduces the mean velocity, which tends to reduce the WSS as well. However, the section reduction between primary and secondary bronchi is such that the WSS increases, despite the smaller mean velocity in the branches.

#### 3.2. Unsteady State without external magnetic field

The unsteady state simulations, without external magnetic field, are carried out by imposing the value of the current intensity to zero. As far as the inlet velocity is concerned, a pulsatile velocity profile is imposed. Figure 4 shows the time variations of the pressure field, on the domain wall, at four different time steps of the respiratory cycle.

The pressure variations during the respiratory cycle are very small, about 1 cm of H<sub>2</sub>O. During the inhalation there is a net flux of air to the lungs, as consequence of the reverse pressure gradient directed from the environment to the lungs, which decreases the pressure from the trachea to the secondary bronchi, as shown in Fig.(4,a). At the end of the inhalation, there is no net mass flow of air between lungs and environment, and the pressure is uniform, as shown in Fig.(4,b). At the end of the inspiratory phase, Fig.(4,c), the pressure

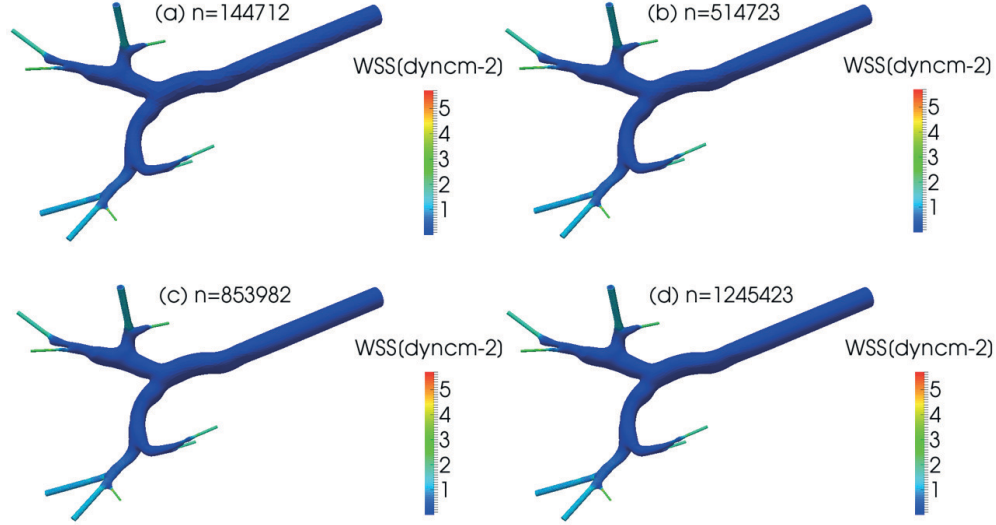


Figure 3: WSS field for the grid independence study in steady state conditions.

increases slightly. At the beginning of the exhalation, a reverse pressure gradient is established between the trachea and the secondary bronchi and air is exhaled, as shown in Fig.(4,d).

Figure 5 presents the nanoparticles coloured by their speed modulus. In Fig.(5,a-b) shows a parabolic-like profile at the beginning of the inhalation, confirming the laminar regime of motion, is shown. The particles with high speed leave the trachea reaching the bronchi, while the particles with low velocity tend to move towards the wall, where they are adsorbed. The adsorption of magnetic nanoparticles in bronchiole lumen has been observed in animal studies [5]. The particles adhesion to the wall is favoured by the low flow rate during the exhalation phase, as confirmed by Fig.(5,d-f).

### 3.3. Unsteady State with external magnetic field

The results of the particle motion in the respiratory system with the magnetic probe turned on are presented in this section. The position of the coil and the target, the probe direction and the intensity of the magnetic induction field, evaluated at 1 cm from the center of the coil, are reported in Table 1.

The maps of the magnetic field on the wall of the lower respiratory tract are shown in Figure ?? at different time steps from the beginning, up to the end

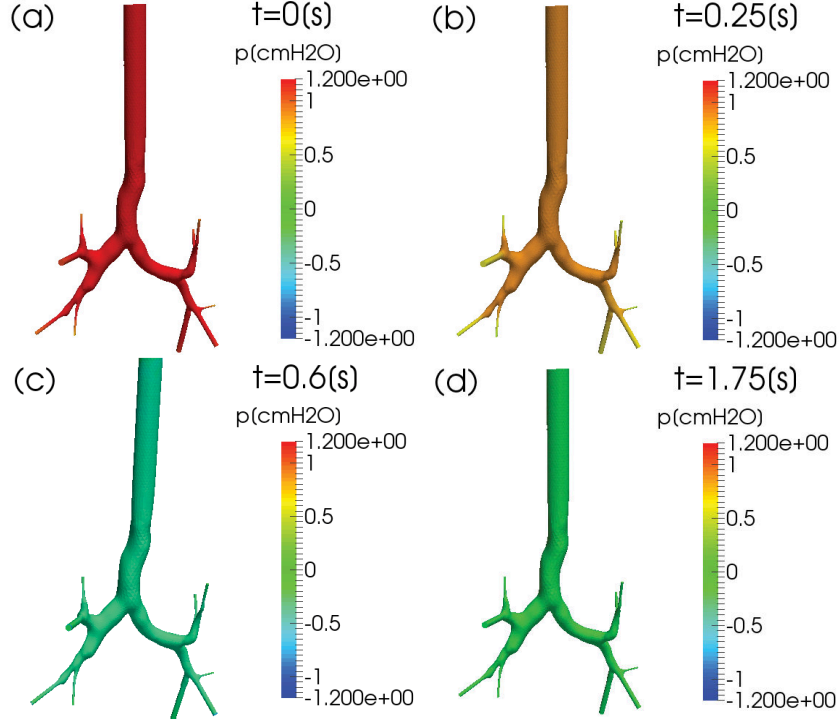


Figure 4: Unsteady Pressure field at different time-steps in absence of external magnetic field.

of the exhalation process, when the particles have filled the entire domain. The maximum value of the magnetic induction field is located on the closer branch to the right upper lobe, where the probe is located, and where the particles tend to be dragged.

The particles path-lines at six instants of time are reported in Figure 7, showing that the flow is transitional. At the beginning of the inhalation, the path-lines are mostly straight, with the presence of few vortexes, especially near the bifurcations, where the velocity gradient becomes higher because of the cross-section reduction. The highest velocity is reached in the trachea, where the environmental air enters into the lungs. Intermittent vortexes form near the bifurcations, due to the curvature changes. At the beginning of the exhalation phase, Fig.(7,b-f), the flow rate is lower and directed towards the trachea, promoting an helical flow with highly tangled path-lines. With this flow-field the time that the particles spend close to the lower respiratory tract wall increases, promoting adsorption. Since the tumor is located in the upper right lobe of the lungs the increased wall adsorption ultimately reduces the efficiency of the technique.

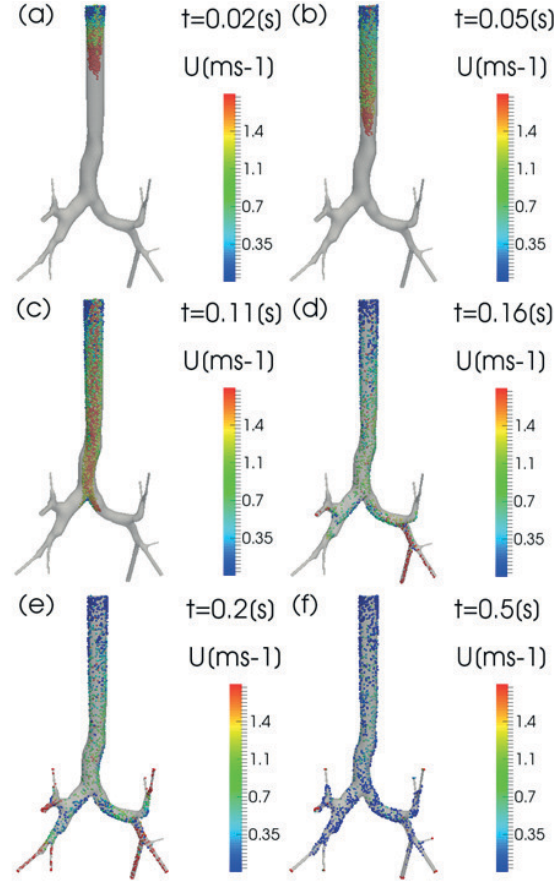


Figure 5: Particles speed at different time-steps in absence of external magnetic field.

Figures 8 and 9 show the influence of the magnetic field on the particles absorption. In order to underline the effect of the magnetic field, the results with the magnetic probe turned off are reported as well.

Figure 8 reports the particle flow rate per unit volume on the different boundaries during the respiratory cycle. In the Trachea and on the domains wall the particle flow rates are of the same order of magnitude. The peak of the exhalation process occurs between 1s and 1.4 s, when the highest flow rate from the lungs to the environment occurs. Figures (9,b,e,f,h,j), show that this phase corresponds to an increase in particle uptake in bronchioles, probably due to the formation of several low speed recirculation regions during the exhalation. The geometry of the bronchi is such that their diameter decreases as they proceed from the trachea to the alveoli. Therefore, since during exhalation the air moves

from the alveoli to the trachea, a flow detachment occurs, causing recirculation regions and promoting the uptake of nanoparticles.

Since the particle flow rate may not show the effectiveness of the use of a rectangular coil in the magnetic targeting, its time integration, corresponding to the total number of particles that crosses a given section from the beginning of the process, is performed.

The probe is pointed towards the upper right lobe of the patients lungs. The uptake of nanoparticles increases in the branches of the lower respiratory tract bended in the frontal direction, Fig.(9,b,e,f,h,j), while it decreases in the branches bended towards the spine, Fig.(9,c,d,g,i). A slight reduction in the particles adhesion to the domain wall is also evidenced.

Despite the increase of particles concentration in the targeted regions, shown in Fig.(9,b), the effect of the magnetic field is not significant. More than 50% of the injected particles adhere to the domain wall when the magnetic probe is turned off, while it is only 47%, when the magnetic probe is turned on. Similarly, the increase of the nanoparticles in the different regions is less than 1%.

This behavior can be due to the high surface-volume ratio of the lower respiratory tract, which inherently increases the probability of adhesion, regardless of the intensity of the magnetic field, and to the geometry of the probe. The magnetic field on the axis of a single square loop decreases quickly from its origin, about 100 times at a distance equal to 2.5 times its width. Considering that the distance between the source and the target is about 12.32 cm, it is clear that this makes the modulus of the magnetic induction considerably low.

#### 4. Conclusions

The present work investigates the dynamics of nanoparticles in air flow during magnetic therapy of a lung tumor, which is an emerging alternative to chemotherapy, because of the reduced side effects. At the best of the authors knowledge, this work represents the first numerical investigation of this technique in a patient-specific lower respiratory tract. The lack of numerical studies is probably due to the complexity of the problem, which couples the air flow with the nanoparticles dynamics under the influence of an external magnetic field. The purpose of this work is to verify numerically the effectiveness of this technique in the treatment of lung cancer. As every numerical study, this work is subject to the limitations due to the input parameters and the model chosen.

The numerical simulations, for steady and unsteady flow, are carried out with the OpenFOAM code in laminar flow, in agreement with [14, 15], with Newtonian viscosity for the air and absence of inter and intraparticle forces, due to the small size of the drug carriers. The simulations are performed in a patient specific geometry, reconstructed from CT slices with VMTK. Three routines are employed in OpenFOAM to implement the BCs for the resistive pressure, the periodic pulsatile velocity profile and the magnetic field from the rectangular coil. Furthermore, a solver coupling the Eulerian MHD of the air with the Lagrangian motion of particles is developed.

One simulation with the magnetic probe turned off and one with the probe turn on are carried out. The results are compared to assess the increase of drug uptake in the lung due to the magneto-therapy and consequently the reduced dispersion in other locations. The rectangular coil, pointing perpendicularly to the tumor is positioned in a specific point, 1 cm above the upper right lobe of the lungs.

The results of the numerical simulations show that, despite the induced magnetic field increases the particle uptake, a small fraction of the total number of particles injected reaches the target. This can be due to the high surface volume ratio of the lower respiratory tract and the design of the magnetic probe.

This conclusion is in contrast with the mathematical model developed for lung alveolus in [30]. This is probably due to the different probe employed, the larger particle diameter ( $5 \mu m$ ) and the higher magnetic field (0.2-2.2 T). Magnetic drug delivery is extremely sensitive to these parameters. Moreover, the drug distribution in different branches is not investigated in [30]. The low performance of the magnetic drug delivery in the present study can be due to three factors: (i) the nanoparticle size; (ii) the magnet-tumor distance; (iii) the probe design. As far as the nanoparticle size is concerned, as shown by Eqs.(18,19) in [29] a low particle diameter increases the acceleration due to Lorentz force, but it also increases the friction. However, because of the low magnetic field applied [48, 49] the effect on the friction is predominant. Therefore, larger particles should increase the effectiveness of the technique, as in [30]. The probe-tumor distance is another factor, which limits the effectiveness of the technique. Unfortunately, this parameter cannot be tuned at will, and in a superficial tumor, the magnetic drug targeting is likely be more effective.

The design of the magnetic probe is another factor that influences the outcome of the procedure. The modulus of the magnetic induction field of a single rectangular coil decreases considerably with the distance from the target, as in the right lung. Being the right lung about 12.32 cm far from the source, the modulus of the magnetic induction field is considerably small. A solution to this problem could be to increase the value of the current intensity flowing in the probe, but this is not possible because higher values of the magnetic field could affect the health of the patient, and is forbidden by law [48, 49]. A solution could be to modify the design of the probe in order to reduce the rate of decay of the magnetic field. A possible configuration could include multiple probes, positioned in appropriate locations.

CFD allows detailed visualization of biological fluid flows, which increases our understanding of natural phenomena, but it has some limitations due to computational resources required to simulate a process in a complex domain. The question then rises as to whether or not the observation time (2 s) is sufficient to judge the effectiveness of the technique. It would be certainly better to extend the simulations to few minutes, but the particle volumetric flow rate in Fig. 9 show negligible differences between the cases. It seems unlikely that the percentage of injected particles, which reach the right lung will significantly increase over time.

Further numerical simulations, in different patient-specific geometries and

364 with different probes, are planned to assess the effectiveness of the therapy in  
365 different conditions.

## 366 5. Acknowledgments

367 This research did not receive any specific grant from funding agencies in the  
368 public, commercial, or not-for-profit sectors. The authors thank the staff of the  
369 Policlinico di Tor Vergata for the support with the biomedical images.

## 370 References

- 371 [1] D. M. Parkin, F. Bray, J. Ferlay, P. Pisani, Global cancer statistics, 2002,  
372 CA: a cancer journal for clinicians 55 (2005) 74–108.
- 373 [2] I. Globocan, Estimated cancer incidence, mortality and prevalence world-  
374 wide in 2012, 2012, (accessed 18 November 2017). [http://globocan.iarc.](http://globocan.iarc.fr/Pages/fact_sheets_cancer.aspx)  
375 [fr/Pages/fact\\_sheets\\_cancer.aspx](http://globocan.iarc.fr/Pages/fact_sheets_cancer.aspx).
- 376 [3] N. Labiris, M. Dolovich, Pulmonary drug delivery. part i: physiological fac-  
377 tors affecting therapeutic effectiveness of aerosolized medications, British  
378 journal of clinical pharmacology 56 (2003) 588–599.
- 379 [4] V. Chandolu, C. R Dass, Treatment of lung cancer using nanoparticle drug  
380 delivery systems, Current drug discovery technologies 10 (2013) 170–176.
- 381 [5] M. P. Garcia, R. M. Parca, S. B. Chaves, L. P. Silva, A. D. Santos, Z. G. M.  
382 Lacava, P. C. Morais, R. B. Azevedo, Morphological analysis of mouse lungs  
383 after treatment with magnetite-based magnetic fluid stabilized with dmsa,  
384 Journal of magnetism and magnetic materials 293 (2005) 277–282.
- 385 [6] F. Gori, A. Boghi, M. Amitrano, Three-dimensional numerical simulation of  
386 the fluid dynamics in a coronary stent, in: ASME International Mechanical  
387 Engineering Congress and Exposition, Proceedings, volume 2, 2009, pp.  
388 407–411.
- 389 [7] F. Gori, A. Boghi, Image-based computational fluid dynamics in a carotid  
390 artery, in: ASME International Mechanical Engineering Congress and Ex-  
391 position, Proceedings, volume 2, 2009, pp. 123–128.
- 392 [8] F. Gori, A. Boghi, Three-dimensional numerical simulation of non-  
393 newtonian blood in two coronary stents, in: 2010 14th International Heat  
394 Transfer Conference, American Society of Mechanical Engineers, 2010, pp.  
395 109–114.
- 396 [9] F. Gori, A. Boghi, Three-dimensional numerical simulation of blood flow  
397 in two coronary stents, Numerical Heat Transfer, Part A: Applications 59  
398 (2011) 231–246.

- 399 [10] A. Boghi, F. Gori, Numerical simulation of blood flow through different  
400 stents in stenosed and non-stenosed vessels, *Numerical Heat Transfer, Part*  
401 *A: Applications* 68 (2015) 225–242.
- 402 [11] I. Di Venuta, A. Boghi, F. Gori, Three-dimensional numerical simulation  
403 of a failed coronary stent implant at different degrees of residual stenosis.  
404 part i: Fluid dynamics and shear stress on the vascular wall, *Numerical*  
405 *Heat Transfer, Part A: Applications* 71 (2017) 638–652.
- 406 [12] A. Boghi, I. Di Venuta, F. Gori, Three-dimensional numerical simulation  
407 of a failed coronary stent implant at different degrees of residual stenosis.  
408 part ii: Apparent viscosity and wall permeability, *Numerical Heat Transfer,*  
409 *Part A: Applications* 71 (2017) 653–665.
- 410 [13] C. Kleinstreuer, Z. Zhang, Z. Li, Modeling airflow and particle trans-  
411 port/deposition in pulmonary airways, *Respiratory physiology & neurobi-*  
412 *ology* 163 (2008) 128–138.
- 413 [14] Z. Zhang, C. Kleinstreuer, Airflow structures and nano-particle deposition  
414 in a human upper airway model, *Journal of computational physics* 198  
415 (2004) 178–210.
- 416 [15] Y. Liu, R. So, C. Zhang, Modeling the bifurcating flow in an asymmetric  
417 human lung airway, *Journal of biomechanics* 36 (2003) 951–959.
- 418 [16] H. Luo, Y. Liu, Modeling the bifurcating flow in a ct-scanned human lung  
419 airway, *Journal of Biomechanics* 41 (2008) 2681–2688.
- 420 [17] R. Calay, J. Kurujareon, A. E. Holdø, Numerical simulation of respiratory  
421 flow patterns within human lung, *Respiratory physiology & neurobiology*  
422 130 (2002) 201–221.
- 423 [18] J. De Backer, W. Vos, C. Gorle, P. Germonpré, B. Partoens, F. Wuyts,  
424 P. M. Parizel, W. De Backer, Flow analyses in the lower airways: patient-  
425 specific model and boundary conditions, *Medical engineering & physics* 30  
426 (2008) 872–879.
- 427 [19] Y. Yin, J. Choi, E. A. Hoffman, M. H. Tawhai, C.-L. Lin, Simulation of  
428 pulmonary air flow with a subject-specific boundary condition, *Journal of*  
429 *biomechanics* 43 (2010) 2159–2163.
- 430 [20] G. Pennati, C. Corsini, D. Cosentino, T.-Y. Hsia, V. S. Luisi, G. Du-  
431 bini, F. Migliavacca, Boundary conditions of patient-specific fluid dynamics  
432 modelling of cavopulmonary connections: possible adaptation of pulmonary  
433 resistances results in a critical issue for a virtual surgical planning, *Interface*  
434 *Focus* 1 (2011) 297–307.
- 435 [21] N. Nowak, P. P. Kakade, A. V. Annapragada, Computational fluid dynam-  
436 ics simulation of airflow and aerosol deposition in human lungs, *Annals of*  
437 *biomedical engineering* 31 (2003) 374–390.



- 438 [22] W. R. Adey, Biological effects of electromagnetic fields, *Journal of cellular*  
439 *biochemistry* 51 (1993) 410–416.
- 440 [23] Z. Saiyed, S. Telang, C. Ramchand, Application of magnetic techniques  
441 in the field of drug discovery and biomedicine, *BioMagnetic Research and*  
442 *Technology* 1 (2003) 1–8.
- 443 [24] M. Larimi, A. Ramiar, A. Ranjbar, Numerical simulation of magnetic  
444 nanoparticles targeting in a bifurcation vessel, *Journal of Magnetism and*  
445 *Magnetic Materials* 362 (2014) 58–71.
- 446 [25] M. D. Tehrani, J.-H. Yoon, M. O. Kim, J. Yoon, A novel scheme for  
447 nanoparticle steering in blood vessels using a functionalized magnetic field,  
448 *IEEE Transactions on Biomedical Engineering* 62 (2015) 303–313.
- 449 [26] M. Larimi, A. Ramiar, A. Ranjbar, Numerical simulation of magnetic  
450 drug targeting with eulerian-lagrangian model and effect of viscosity mod-  
451 ification due to diabetics, *Applied Mathematics and Mechanics* 37 (2016)  
452 1631–1646.
- 453 [27] M. Momeni Larimi, A. Ramiar, A. A. Ranjbar, Magnetic nanoparticles  
454 and blood flow behavior in non-newtonian pulsating flow within the carotid  
455 artery in drug delivery application, *Proceedings of the Institution of Me-*  
456 *chanical Engineers, Part H: Journal of Engineering in Medicine* 230 (2016)  
457 876–891.
- 458 [28] S. Kenjereš, B. Righolt, Simulations of magnetic capturing of drug carriers  
459 in the brain vascular system, *International Journal of Heat and Fluid Flow*  
460 35 (2012) 68–75.
- 461 [29] A. Boghi, F. Russo, F. Gori, Numerical simulation of magnetic nano drug  
462 targeting in a patient-specific coeliac trunk, *Journal of Magnetism and*  
463 *Magnetic Materials* 437 (2017) 86–97.
- 464 [30] A. Krafcik, P. Babinec, I. Frollo, Computational analysis of magnetic field  
465 induced deposition of magnetic particles in lung alveolus in comparison to  
466 deposition produced with viscous drag and gravitational force, *Journal of*  
467 *Magnetism and Magnetic Materials* 380 (2015) 46–53.
- 468 [31] D. A. Steinman, Image-based computational fluid dynamics modeling in  
469 realistic arterial geometries, *Annals of biomedical engineering* 30 (2002)  
470 483–497.
- 471 [32] L. Antiga, B. Ene-Iordache, L. Caverni, G. P. Cornalba, A. Remuzzi, Geo-  
472 metric reconstruction for computational mesh generation of arterial bifur-  
473 cations from ct angiography, *Computerized Medical Imaging and Graphics*  
474 26 (2002) 227–235.

- [33] L. Antiga, M. Piccinelli, L. Botti, B. Ene-Iordache, A. Remuzzi, D. A. Steinman, An image-based modeling framework for patient-specific computational hemodynamics, *Medical & biological engineering & computing* 46 (2008) 1097–1112.
- [34] D. F. Young, B. R. Munson, T. H. Okiishi, W. W. Huebsch, A brief introduction to fluid mechanics, John Wiley & Sons, 2010.
- [35] S. Elghobashi, On predicting particle-laden turbulent flows, *Applied scientific research* 52 (1994) 309–329.
- [36] E. Tzirtzilakis, V. Sakalis, N. Kafoussias, P. Hatzikonstantinou, Biomagnetic fluid flow in a 3d rectangular duct, *International Journal for Numerical Methods in Fluids* 44 (2004) 1279–1298.
- [37] M. Arruebo, R. Fernández-Pacheco, M. R. Ibarra, J. Santamaría, Magnetic nanoparticles for drug delivery, *Nano today* 2 (2007) 22–32.
- [38] S. Seino, Y. Matsuoka, T. Kinoshita, T. Nakagawa, T. A. Yamamoto, Dispersibility improvement of gold/iron-oxide composite nanoparticles by polyethylenimine modification, *Journal of Magnetism and Magnetic Materials* 321 (2009) 1404–1407.
- [39] M. Hassan, A. Zeeshan, A. Majeed, R. Ellahi, Particle shape effects on ferrofluids flow and heat transfer under influence of low oscillating magnetic field, *Journal of Magnetism and Magnetic Materials* 443 (2017) 36–44.
- [40] A. Zeeshan, M. Hassan, R. Ellahi, M. Nawaz, Shape effect of nanosize particles in unsteady mixed convection flow of nanofluid over disk with entropy generation, volume 231, SAGE Publications Sage UK: London, England, 2017, pp. 871–879.
- [41] A. Majeed, A. Zeeshan, T. Hayat, Analysis of magnetic properties of nanoparticles due to applied magnetic dipole in aqueous medium with momentum slip condition, *Neural Computing and Applications* (2017) 1–9.
- [42] L. Schiller, Z. Naumann, A drag coefficient correlation, *Vdi Zeitung* 77 (1935) 51.
- [43] G. J. Metzger, P.-F. van de Moortele, C. Akgun, C. J. Snyder, S. Moeller, J. Strupp, P. Andersen, D. Shrivastava, T. Vaughan, K. Ugurbil, et al., Performance of external and internal coil configurations for prostate investigations at 7 t, *Magnetic resonance in medicine* 64 (2010) 1625–1639.
- [44] F. Dughiero, E. Baake, M. Forzan, V. Nemkov, R. Ruffini, R. Goldstein, J. Jackowski, T. DeWeese, R. Ivkov, Magnetic field generating inductor for cancer hyperthermia research, *COMPEL - The international journal for computation and mathematics in electrical and electronic engineering* 30 (2011) 1626–1636.

- 513 [45] A. S. Lübke, C. Alexiou, C. Bergemann, Clinical applications of magnetic  
514 drug targeting, *Journal of Surgical Research* 95 (2001) 200–206.
- 515 [46] A. S. Lübke, C. Bergemann, H. Riess, F. Schriever, P. Reichardt,  
516 K. Possinger, M. Matthias, B. Dörken, F. Herrmann, R. Gürtler, et al.,  
517 Clinical experiences with magnetic drug targeting: a phase i study with 4-  
518 epidoxorubicin in 14 patients with advanced solid tumors, *Cancer research*  
519 56 (1996) 4686–4693.
- 520 [47] M. Misakian, Equations for the magnetic field produced by one or more  
521 rectangular loops of wire in the same plane, *Journal of research of the*  
522 *National Institute of Standards and Technology* 105 (2000) 557–564.
- 523 [48] E. Council, Recommendation on the limitation of exposure of the general  
524 public to electromagnetic field (0 hz to 300 ghz), *Official Journal of the*  
525 *European Communities* 199 (1999) 59–70.
- 526 [49] F. C. Commission, Evaluating compliance with FCC guidelines for human  
527 exposure to radiofrequency electromagnetic fields, volume 65, *OET Bulletin*,  
528 1997.

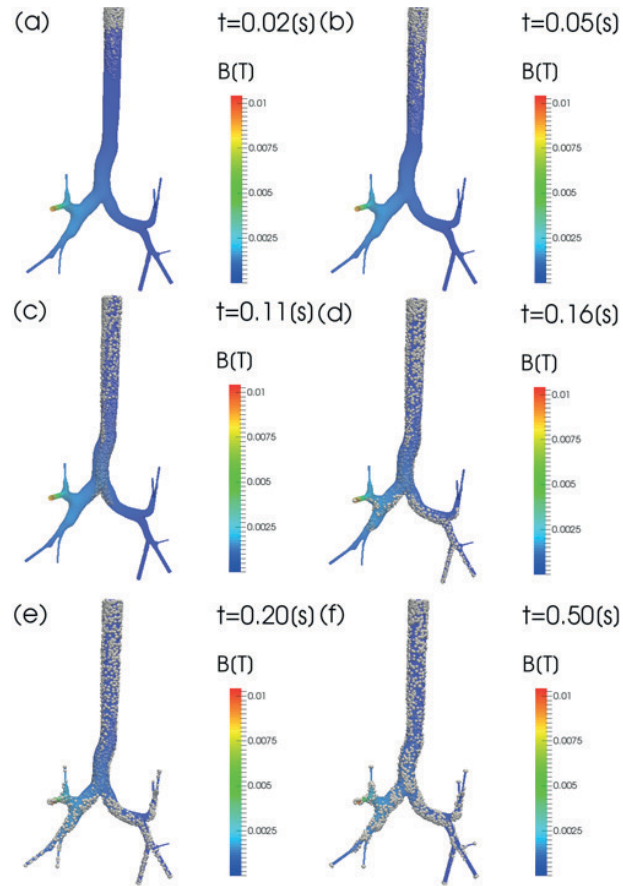


Figure 6: Magnetic Induction Field and particle positions at different time steps, with external magnetic field.

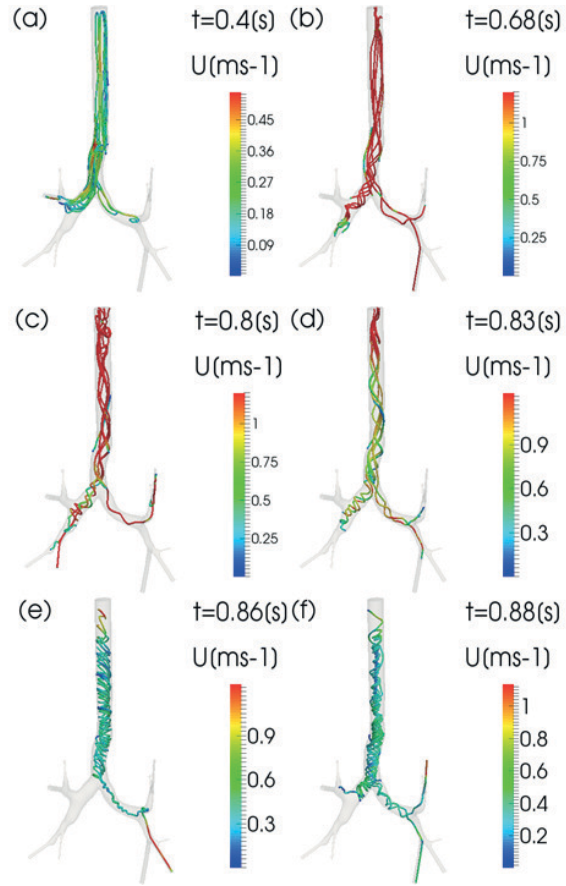


Figure 7: Velocity Field and velocity streamlines at different time steps with external magnetic field.

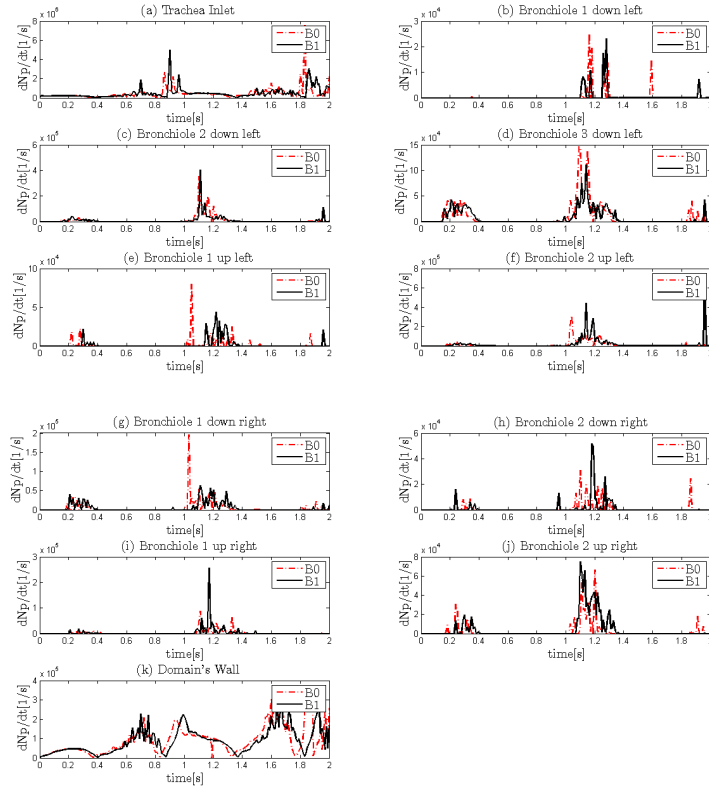


Figure 8: Particle volumetric flow rate per unit volume vs time for the two different conditions. B0 = magnetic field off; B1 = magnetic field on.

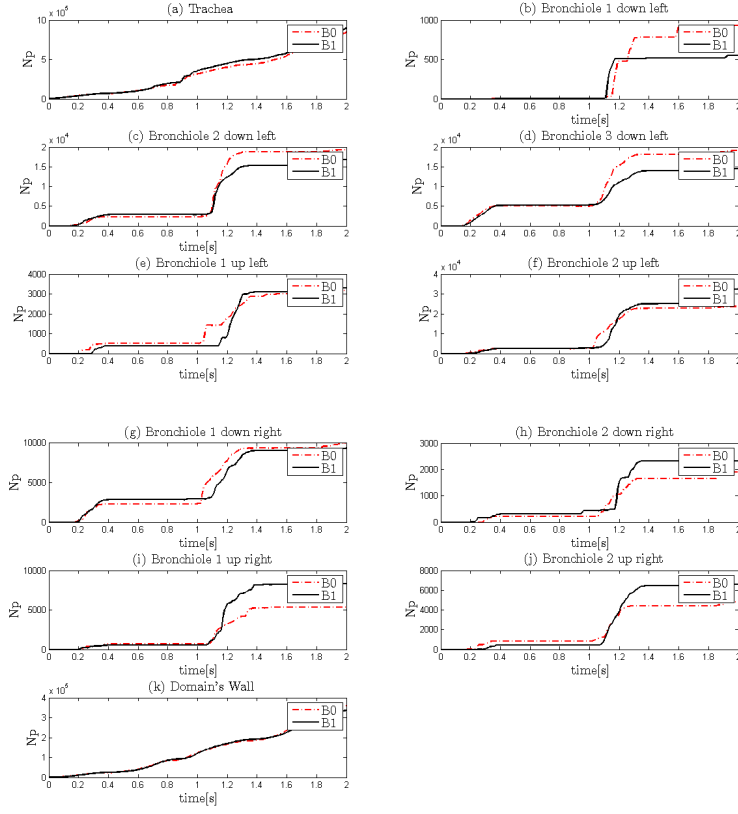


Figure 9: Particle number vs time for the two different conditions. B0 = magnetic field off; B1 = magnetic field on.

# Numerical simulation of magnetic nano drug targeting in patient-specific lower respiratory tract

Russo, Flavia

2017-12-02

Attribution-NonCommercial-NoDerivatives 4.0 International

---

Russo F, Boghi A, Gori F. (2018) Numerical simulation of magnetic nano drug targeting in patient-specific lower respiratory tract. *Journal of Magnetism and Magnetic Materials*, Volume 451, April 2018, pp. 554-564

<https://doi.org/10.1016/j.jmmm.2017.11.118>

*Downloaded from CERES Research Repository, Cranfield University*